Spatially controlled octahedral rotations and metal-insulator transitions in NdNiO3/SrTiO3 superlattices

Binbin Chen, Nicolas Gauquelin, Robert J Green, Jin Hong Lee, Cinthia Piamonteze, Matjaž Spreitzer, Daen Jannis, Johan Verbeeck, M. Bibes, Mark Huijben, et al.

Spatially controlled octahedral rotations and metal-insulator transitions in $NdNiO_3/SrTiO_3$ superlattices

Binbin Chen,[1] Nicolas Gauquelin,[2] Robert J. Green,[3,4] Jin Hong Lee,[5] Cinthia Piamonteze,[6] Matjaž Spreitzer,[7] Daen Jannis,[2] Johan Verbeeck,[2] Manuel Bibes,[5] Mark Huijben,[1] Guus Rijnders,[1] Gertjan Koster[1]*

[1]MESA+ Institute for Nanotechnology, University of Twente, 7500 AE Enschede, The Netherlands
[2]Electron Microscopy for Materials Science (EMAT), University of Antwerp, 2020 Antwerp, Belgium
[3]Department of Physics and Engineering Physics, University of Saskatchewan, 116 Science Pl, Saskatoon, Saskatchewan S7N 5E2, Canada
[4]Stewart Blusson Quantum Matter Institute, University of British Columbia, 111-2355 E Mall, Vancouver, British Columbia V6T 1Z4, Canada
[5]Unité Mixte de Physique, CNRS, Thales, Université Paris-Saclay, 91767 Palaiseau, France
[6]Swiss Light Source, Paul Scherrer Institute, 5232 Villigen PSI, Switzerland
[7]Advanced Materials Department, Jožef Stefan Institute, 1000 Ljubljana, Slovenia

Abstract

The properties of correlated oxides can be largely manipulated by forming short-period superlattices (SLs) since the layer thicknesses are comparable with the typical length scales of the involved correlations and interface effects. Herein, we studied the metal-insulator transitions (MITs) in tetragonal $NdNiO_3/SrTiO_3$ SLs by atomically controlling the $NdNiO_3$ layer thickness, n in unit cell, spanning the length scale of the interfacial octahedral coupling. Atomic resolution scanning transmission electron microscopy reveals a crossover from a modulated octahedral superstructure at n = 8 to a uniform non-tilt pattern at n = 4, which is accompanied by a drastically weakened insulating ground state. Upon further reducing n the predominant dimensionality effect continuously raises the MIT temperature, while leaves the antiferromagnetic transition temperature unaltered down to n = 2. Remarkably, the MIT and antiferromagnetic transition can be enhanced by imposing a sufficiently large strain even with strongly suppressed octahedral rotations. Our results shed new insights into the decoupled nature of the MIT and antiferromagnetic transition in rare-earth nickelates and demonstrate the relevance for the control of oxide functionalities at reduced dimensions.

The ubiquitous electron-lattice coupling in perovskite oxides enables us to tune their functionalities by virtue of structural engineering.[1–10] In addition to the well-established strain approach, engineering of the oxygen octahedral rotations (OOR) has been recognized as another effective tool since both the electronic bandwidth and magnetic exchange interaction in oxides are sensitive to the changes of the M-O-M (M, transition metal ion) bond angle.[3–10] At the interface between two perovskites, the corner-shared octahedral network has to rearrange to maintain the connectivity, known as the octahedral proximity effect.[3] Such an effect is usually confined within several unit cells (uc) and rapidly decays away from the interface,[3–10] in contrast to the long-range effect up to tens of nanometers for strain engineering.[1,2] The former requires only subtle and gradual bond angle changes, whereas strain relaxation usually involves the formation of dislocations. By forming short-period superlattices (SLs), the interfacial OOR coupling can be extended throughout the entire film, thus creating novel structural phases with distinct properties from the individual components.[7,11,12] Importantly, the OOR can be further manipulated in SLs by altering the relative thickness ratio of the component layers or selectively utilizing a tilt-control layer, offering extra tuning "knobs".[7,9,12] However, when the layer thickness is reduced down to a few uc in SLs, a dimensional effect comes into play and usually reduces the bandwidth.[13–19] The competition between the OOR and dimensional effects remains rarely explored,[20,21] but is crucial for the rational control over oxide functionalities at the atomic scale.

Rare-earth nickelates RNiO$_3$ have received continuous attention not only because of the puzzling physics but also for the potential to design "Mottronics" devices.[22,23] Except for R = La, RNiO$_3$ displays a first-order metal-insulator transition (MIT) which can be systematically tuned by changing rare-earth cations. Concurrent with the MIT, a structural transition from orthorhombic (Pbnm) to monoclinic ($P2_1/c$) symmetry occurs due to the breathing distortions of the NiO$_6$ octahedra. This MIT is accompanied by a paramagnetic to antiferromagnetic transition for R = Pr and Nd, although the transitions

are well separated for the smaller rare-earth ions. The mechanism for this temperature-driven MIT has been a long-standing debate.[24–30] Recently, resonant inelastic X-ray scattering spectroscopy revealed a negative charge transfer energy and oxygen ligand holes ($\underline{L}$) in $NdNiO_3$ (NNO),[31] pointing to a theoretically predicted bond disproportionation scenario.[25] The ground state is then described as alternatively arranged Ni $3d^8$ and Ni $3d^8\underline{L}^2$ sites, which is associated with the breathing mode of the NiO_6 octahedra.[30] The two inequivalent Ni-O bonds can also account for the peculiar antiferromagnetic order at low temperatures.[22] More recently, the intimate competition between the two main structural distortions in $RNiO_3$, namely the breathing mode and the OOR, has been unveiled by first-principle calculations, where a certain magnitude of OOR can trigger the breathing mode and induce the MIT.[29]

$RNiO_3$ at reduced dimensions is of interest as a planar orbital order, similar to high-temperature superconducting cuprates, has been predicted.[32,33] Aside from the orbital control, an emergent antiferromagnetic order, competing electronic phases and enhanced charge-order propensity have also been reported in artificially confined $RNiO_3$ heterostructures.[13,15,34,35] In the present work, the combined effects of the OOR and spatial confinement on the MIT were studied in NNO/$SrTiO_3$ (STO) SLs via digitally varying the NNO layer thickness, n in uc. The evolution of the OOR behavior has been revealed by scanning transmission electron microscopy (STEM). We observed a nonmonotonic variation of the MIT temperature (T_{MIT}) as a function of n because of the competition between the OOR and the dimensional crossover. On the other hand, the antiferromagnetic transition temperature (T_N) is found to be mainly controlled by the Ni-O-Ni bond angle and Ni-O bond length, but insensitive to the dimensional reduction. The distinct response of the MIT and the antiferromagnetic transition to dimensionality offers great opportunities to engineer novel electronic phases in short-period oxide SLs.

Results

Fabrication of NNO/STO SLs. The NNO/STO SLs, $[n/4]_{10}$ were fabricated on $(001)_{pc}$-oriented (pc, pseudocubic) $NdGaO_3$ (NGO) substrates by means of pulsed laser deposition monitored with reflection high-energy electron diffraction (RHEED) (Supplementary Fig. 1). The STO layer thickness was set to 4-uc and the NNO/STO bilayer was repeated 10 times to form the SL. In bulk, NNO is orthorhombic at room temperature showing the typical $GdFeO_3$-type distortion. The OOR pattern can be depicted as $a^+b^-b^-$ in Glazer notation, where the superscript + (-) indicates the adjacent octahedra rotate in-phase (out-of-phase) along the corresponding pseudocubic axis (Fig. 1a). Hereafter, we use the pseudocubic indices for NGO, with *a*, *b* and *c* corresponding to the [001], [1-10] and [110] axes of the orthorhombic lattice. According to first-principle calculations, the combination of out-of-phase and in-phase rotations can drive anti-polar displacements of the A-site cations to optimize the oxygen coordination,[36] as can be seen from the projection along the *b* axis of NNO. In this work, we used the A-site displacements as a relative measure of the OOR in the NNO layer considering the high accuracy in determining Nd^{3+} positions from STEM.[7,9,37] Unlike orthorhombic NNO, STO is cubic without any OOR and A-site displacements (Fig. 1b). The symmetry mismatch at the heterointerface can significantly alter the OOR in the near-interface region and tune its properties.[3,5] Fig. 1c shows the high-resolution θ-2θ X-ray diffraction (XRD) scans around the NGO(220) peak for SLs with various thicknesses of NNO. The satellite peaks, due to the chemical modulation along the growth direction, as well as the thickness fringes can be clearly identified for all SLs, attesting the presence of abrupt interfaces and smooth surfaces. The period distance calculated from the satellite peaks agrees well with the expected NNO and STO layer thicknesses. While reducing the NNO layer thickness, the main peak gradually shifts to lower angles. The extracted out-of-plane lattice parameter, *c* is plotted in Fig. 1d. The NNO single film shows c = 3.79 Å, smaller than the bulk value (3.81 Å) owing to the in-plane tensile strain, which should be

similar for all samples. In NNO/STO SLs, c gradually increases from 3.84 Å to 3.91 Å as n decreases from 8 to 2 uc. This can be understood by the increasing contribution from the compressively strained STO layer (3.905 Å in bulk). The systematic change of c is consistent with the varied composition of SLs. Fig. 1e and f show the surface morphology of the NGO substrate and the n = 8 SL. The step-terrace surface structure of NGO with unit cell height steps is well preserved after growth of the full SL, confirming the high crystalline ordering of our samples.

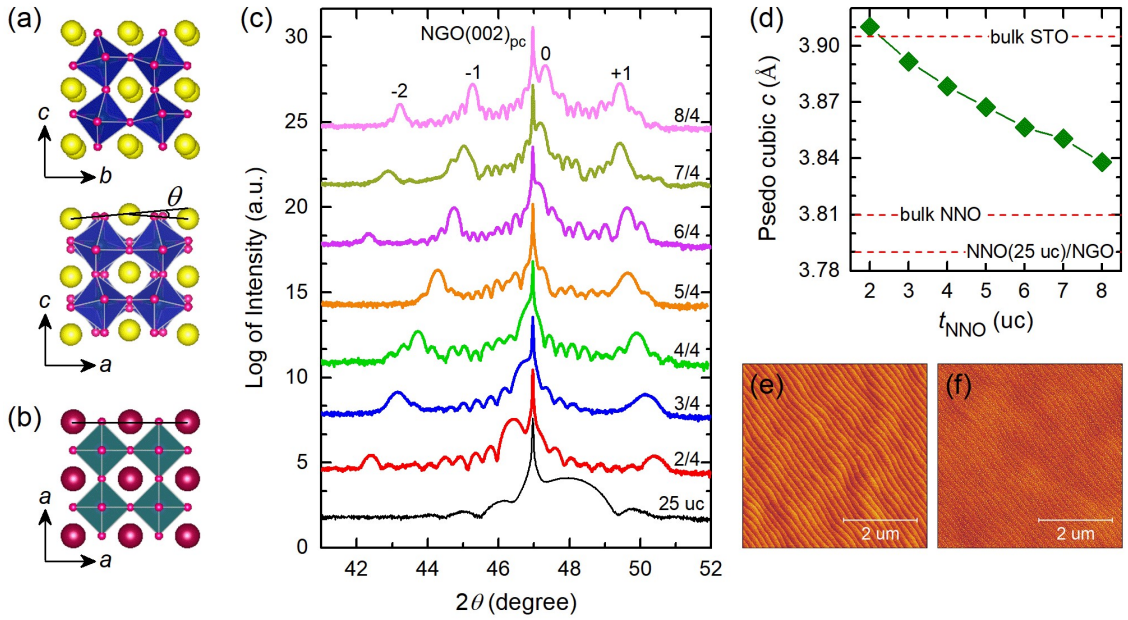

Fig. 1 Structural characterization of NNO/STO SLs. The crystal structures of NNO and STO components are schematically shown in (a) and (b), respectively. The A-site anti-polar displacement is clearly visible in the orthorhombic NNO as characterized by the deviation angle θ, but absent in the cubic STO. (c) High-resolution XRD θ-2θ scans around NGO(002)$_{pc}$ peak for the NNO/STO SLs with various thicknesses of NNO. (d) Pseudocubic lattice constant c as a function of the NNO layer thickness. (e,f) AFM images of the single-terminated NGO substrate and the n = 8 SL, respectively.

Thickness-dependent structural evolution in NNO/STO SLs. To gain insight into the structural modulations induced by the epitaxial constraint, we conducted reciprocal space mapping (RSM) measurements on the pseudocubic (013), (103), (0-13) and (-103) reflections of a 25-uc thick NNO film and a 8/4 SL, as shown in Fig. 2. The

reflections from the substrate and films share the same in-plane Q_X value, indicative of coherently strained states.

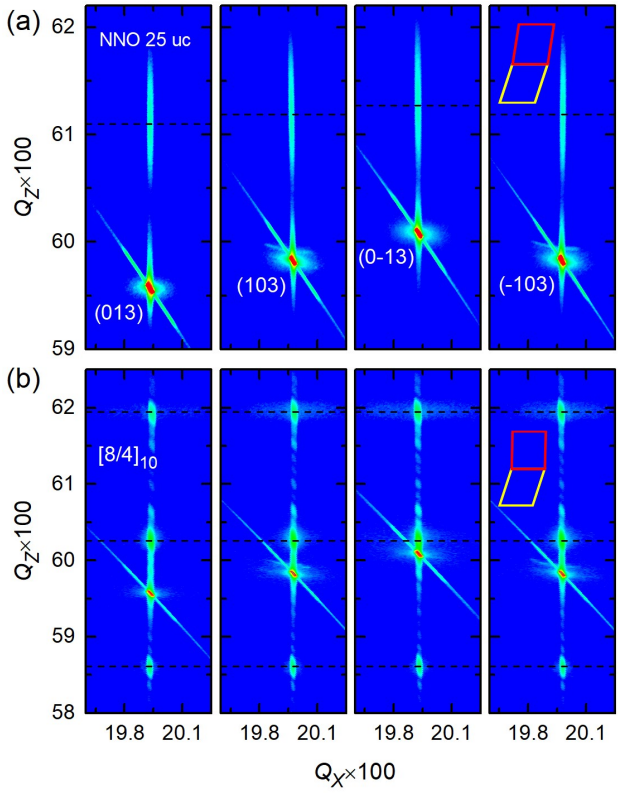

Fig. 2 Tetragonal symmetry of NNO/STO SLs. RSMs around pseudocubic (013), (103), (0-13) and (-103) reflections measured from NNO single film (a) and NNO/STO SL with n = 8 (b). The schematic insets show the shear distortion of the pseudocubic lattice in the film or SL (red) and the substrate (yellow) as extracted from the RSMs.

Therefore, strain effects cannot be responsible for the variations of MIT observed within the NNO/STO SL series,[17] as will be discussed later. For the 25-uc NNO film, the four reflections show different out-of-plane Q_Z values, similar to the orthorhombic NGO substrate. As schematically shown in the inset of Fig. 2, a shear distortion angle of ~0.26º is deduced for the pseudocubic unit cell of NNO. The angle is smaller than that of NGO (~0.73º) due to the larger Goldschmidt tolerance factor.[3,4] According to previous reports, the OOR along the out-of-plane c axis is suppressed in the NNO film to accommodate the in-plane tensile strain (~1.26%).[38,39] The OOR pattern therefore can be assigned as $a^+b^-c^-$. In contrast to the NNO single film, no Q_Z shifts were observed for the 8/4 SL, pointing to

a tetragonal symmetry.[10,20,40] This indicates a change in the crystal symmetry from orthorhombic to tetragonal as we intercalate NNO with ultrathin STO layers. An analogous structural change has also been reported in $SrRuO_3$ films grown on STO as the thickness is reduced below a critical value.[40] The tetragonal phase is ascribed to the suppressed OOR along the in-plane axes as evidenced by STEM and half-order XRD measurements.[5,40,41] The crystal symmetry change is also manifested as a large jump of the out-of-plane lattice parameter from the NNO single film to the 8/4 SL as shown in Fig. 1d.[10] For the SLs with thinner NNO layers, the RSMs show the same features as the 8/4 SL (Supplementary Fig. 2). Given the fact that XRD measurements provide average structural information over the samples, we performed atomically resolved STEM measurements to reveal more delicate changes of the OOR within the NNO/STO SLs.

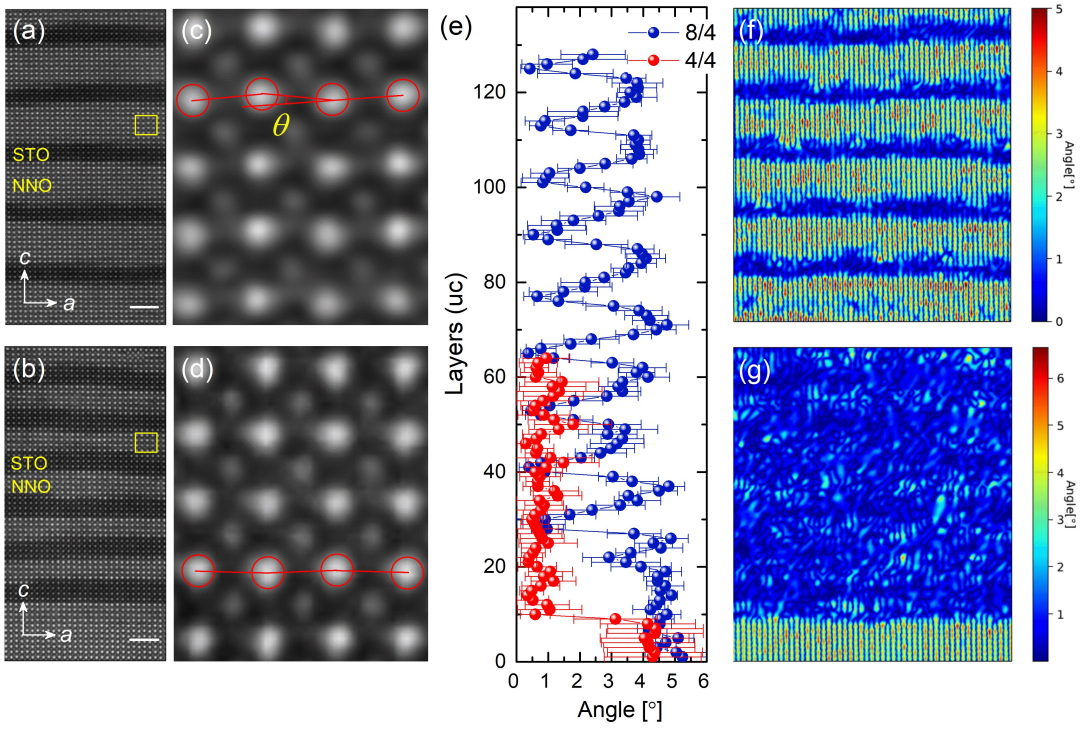

Fig. 3 STEM characterizations of OOR in NNO/STO SLs. (a,b) STEM-HAADF images of NNO/STO SLs with n = 8 and n = 4, respectively. Scale bar, 2 nm. The corresponding enlarged images are shown in (c) and (d) to highlight the A-site anti-polar displacements. A deviation angle θ is defined as described in the main text. (e) Layer-resolved deviation angle θ of the SLs with n = 4 and n = 8. (f,g) cross-sectional mapping of θ in SLs with n = 4 and n = 8, respectively.

Fig. 3a and b show the high-angle annular dark field (HAADF)-STEM images of the SLs with 8- and 4-uc NNO, respectively. Due to the large difference in atomic number between Sr and Nd atoms, the NNO and STO layers can be readily defined from the Z-contrast images as well as the electron energy loss spectroscopy (EELS) color maps (Supplementary Fig. 3). Fig. 3c and d show the enlarged images of the NNO layer in the corresponding SLs to highlight the displacements of Nd^{3+}. We define θ as the deviation of the angle between three successive Nd^{3+} cations along the a axis from 180º. Note that θ is proportional to the OOR.[7,9,37] We find that the 8/4 SL shows pronounced anti-polar displacements of Nd^{3+}, which becomes negligible in the 4/4 SL. The quantified measure of θ is carried out along the growth direction as summarized in Fig. 3e. A clear modulation of θ is observed in the 8/4 SL. The non-interfacial region of NNO shows a maximum θ of ~3.5º which decays to ~0.5º over ~3 uc close to the NNO/STO interface. The induced anti-polar displacement ($\theta \sim 0.5$º) in the otherwise cubic STO is consistent with the previous report on the STO/$GdTiO_3$ interface.[37] For the 4/4 SL, we observe a uniform θ of ~0.5º throughout the SL. Therefore, the coherence length of the interfacial OOR coupling is around ~2 uc on the NNO side, which is comparable to that of $SrIrO_3$/STO and $La_{0.7}Sr_{0.3}MnO_3$/STO interfaces.[21,42] Fig. 3f and g show the cross-sectional mapping of θ. The modulated θ in the 8/4 SL is in sharp contrast with the nearly homogenous distribution of θ in the 4/4 SL. The almost quenched A-site anti-polar displacement indicates $a^0a^0c^-$ for the 4/4 SL.[43] This means the OOR along the in-plane axes is further blocked by reducing the NNO layer thickness.

Thickness dependent MITs in NNO/STO SLs. The modifications to the structural ordering within the NNO/STO SLs are expected to cause significant variations to the transport properties. Fig. 4a shows the temperature dependent resistivity curves of the NNO/STO SLs as well as a 25-uc thick NNO film for reference. The resistivity at 300 K [$\rho(T = 300$ K)] and 10 K [$\rho(T = 10$ K)] are plotted against NNO layer thickness (n) in Fig.

4b. The resistivity is calculated by considering the sole contribution from NNO layers since the deposition at high oxygen pressure produces insulating STO layers.[44] At first glance, as n is reduced, $\rho(T = 300\ \mathrm{K})$ gradually increases whereas $\rho(T = 10\ \mathrm{K})$ shows a non-monotonic variation (see Fig. 4b). As we will discuss below, the complex evolution of the low-temperature insulating states is related to the competition between the OOR and spatial confinement. The NNO film undergoes a sharp MIT as the temperature decreases below 176 K, which is 24 K lower than the bulk value (~200 K).[22] The drop of T_{MIT} has been ascribed to the tensile strain resulting from the lattice mismatch.[2,45] The resistivity shows a change of four orders of magnitude across the MIT, indicative of the high crystallinity and optimal oxygen stoichiometry of our film.[45,46] In the 8/4 SL T_{MIT} drastically decreases to 128 K. Also, the low-temperature insulating state is suppressed as manifested by the sharp decline of $\rho(T = 10\ \mathrm{K})$ shown in Fig. 4b. This is related to the suppression of orthorhombic distortions as evidenced by the RSM results in Fig. 2. The suppressed OOR along the in-plane axes stretches the Ni-O-Ni bond and boosts the bandwidth as revealed by X-ray absorption measurements.[9,10] Note that the transition hysteresis is similar to the NNO single film, which implies that the percolation behavior across the MIT is not interrupted in the n = 8 SL.[22] However, the thermal hysteresis is markedly weakened upon reducing n from 8 to 6 uc. Meanwhile, the T_{MIT} gradually increases from 128 to 162 K accompanied by a rise of $\rho(T = 10\ \mathrm{K})$. This is ascribed to the dimensionality effect which should stabilize the insulating phase by blocking the interlayer electron hopping.[14–17] As a result, the region with coexisting metallic and insulating phases gradually vanishes.[17] Most strikingly, as n is further reduced, we observe an unexpected decline of T_{MIT} from 162 K at 6 uc to 142 K at 5 uc, concurrent with a sudden drop of $\rho(T = 10\ \mathrm{K})$. The result is somewhat counterintuitive since the dimensionality effects are expected to raise T_{MIT} continuously by promoting the insulating state.[17] We suggest the delicate changes of OOR in the SLs to be responsible for this anomaly. As n is reduced below a critical thickness (~6 uc), the OOR of the SLs

changes to $a^0a^0c^-$ by quenching the in-plane OOR given the limited coherence length of the interfacial OOR coupling effects.[3,21,42] The quenched in-plane octahedral tilting can suppress the breathing mode instabilities in NNO and then weaken the MIT.[29]

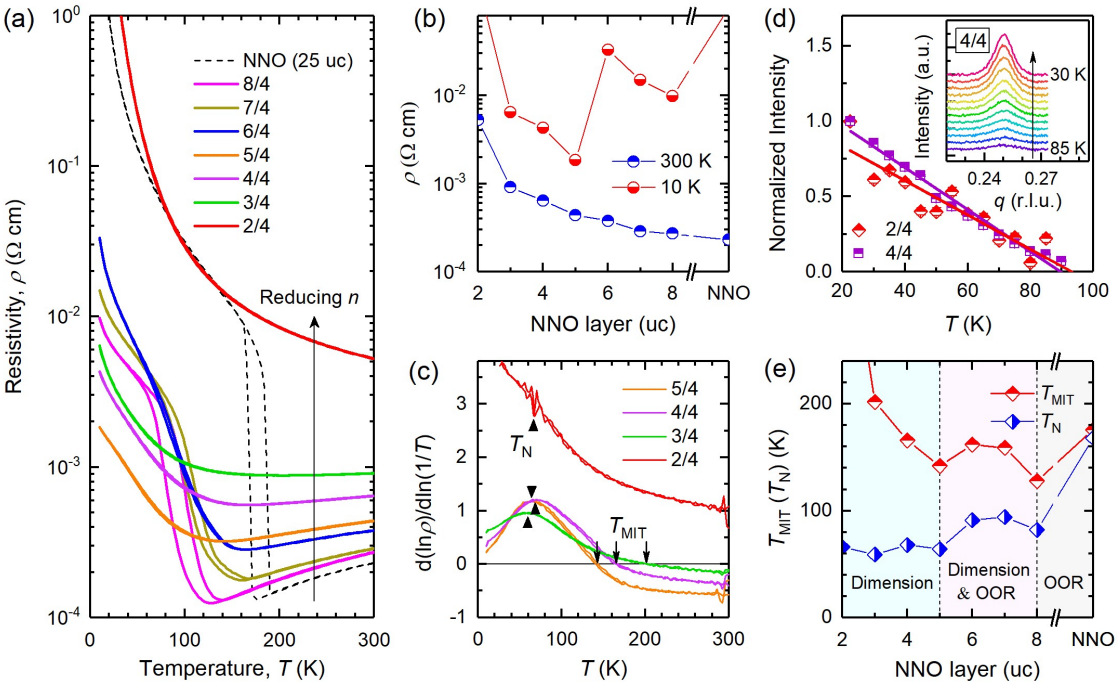

Fig. 4 Thickness-dependent MITs in NNO/STO SLs. (a) Temperature dependent resistivity (ρ-T) curves of NNO/STO SLs with various n, along with a 25-uc-thick NNO single film for comparison. (b) The resistivities at 300 K and 10 K as a function of NNO layer thickness. (c) The $d(\ln\rho)/d\ln(1/T)$-T plots for SLs with n = 2, 3, 4 and 5. The derived T_{MIT} and T_N are marked by arrows and triangles, respectively. (d) Temperature dependent integrated intensity of the q = (¼, ¼, ¼) reflection for SLs with n = 2 and 4 measured by RMD. The linear fitting is used to extract the onset temperature of the antiferromagnetic order. The inset shows the isothermal rocking curves around the q = (¼, ¼, ¼) reflection taken from SL with n = 4. The measurements were performed from 30 to 85 K with a step of 5 K. (e) Phase diagram of NNO/STO SLs as a function of n. Here T_N is derived from the transport measurements. PM, PI and AFI denote paramagnetic metal, paramagnetic insulator and antiferromagnetic insulator.

Upon decreasing n below 5 uc, the OOR of the SLs should be unchanged and the dominated dimensionality effects dramatically increase the T_{MIT} (see Fig. 4c). For the n = 2 SL, it exhibits insulating behavior in the entire temperature range measured. The temperature dependent resistivity curve can be well fitted with the two-dimensional

variable range hopping conduction model (Supplementary Fig. 4). This attests to the dimensional crossover as we reduce the NNO layer thickness, and also indicates that the inevitable disorder effect plays a role in the MIT at the ultrathin limits.[35]

The altered OOR should also have a profound impact on the antiferromagnetic transitions of the SLs. Here, the peak position of the $\ln\rho/\ln(1/T)$-T plot has been used to track T_N in RNiO$_3$.[2,47] As can be seen from Fig. 4e, T_N nearly coincides with T_{MIT} for NNO single film, while they are well separated for all SLs. The decoupling of MIT and spin ordering has also been reported for other RNiO$_3$-based heterostructures and SLs with different boundary conditions.[2,9,48,49] The suppressed OOR along in-plane axes leads to a decrease of T_N from ~168 K for the 25-uc NNO film to ~82 K for the n = 8 SL, following the trend in bulk RNiO$_3$ phase diagram.[22] As n decreases from 8 to 6 uc, T_N hardly changes due to the slightly altered OOR in this thickness range. Remarkably, the further blocking of the in-plane OOR reduces T_N from ~91 K to ~64 K as n decreases from 6 to 5 uc. It is interesting to note that T_N remains nearly constant for $n \leq 5$ in contrast to a rapidly increasing T_{MIT} (see Fig. 4c). For the insulating SL with n = 2, the antiferromagnetic transition is manifested as an anomaly around ~68 K of the $\ln\rho/\ln(1/T)$-T curve, corresponding to a kink visualized from the enlarged resistivity curve (Supplementary Fig. 5). This resembles RNiO$_3$ with small rare-earth ions.[47] To further ascertain the antiferromagnetic transitions in SLs with ultrathin NNO, we performed X-ray resonant magnetic diffraction (RMD) measurements for SLs with n = 2 and 4 (see Fig. 4d and Fig. S5). The integrated peak intensity of the q = (¼, ¼, ¼) reflection linearly decreases with increasing temperature. This is different from NNO single films which follow the mean field model.[2,49] The linear extrapolations give onset temperatures of ~93 K for n = 2 and ~90 K for n = 4 SL. The values are ~30 K higher than those derived from transport measurements. Such discrepancy arises because RMD and derivative of resistivity characterize different stages of the antiferromagnetic transition. While RMD probes the onset of antiferromagnetic domains, the deflection point from $\ln\rho/\ln(1/T)$-T

plot marks the percolation threshold. For two-dimensional systems, the percolation occurs when the volume fraction of the antiferromagnetic insulating phase reaches 50%.[50] Importantly, the RMD results strengthen the conclusion that T_N in SLs with $n \leq 5$ is stable against further reducing NNO layer thickness down to 2 uc.

Taken together, the results suggest that T_N is mainly governed by the Ni-O-Ni bond angle and insensitive to the dimensional crossover in NNO/STO SLs. The argument is supported by the report on NNO/$NdAlO_3$ (NAO) SLs, where a thickness-independent T_N of ~150 K is observed even with a NNO layer of 2-uc thick.[49] Noteworthy, the T_N of NNO/NAO SLs is ~80 K higher than the NNO/STO SLs. This large gap can be understood as a result of the difference in Ni-O-Ni bond angles. Since NAO is orthorhombic with a large magnitude of OOR, the interfacial OOR coupling is expected to yield more bended Ni-O-Ni bonds in NNO/NAO SLs than NNO/STO SLs.[3,4] The quasi-two dimensional antiferromagnetism preserved in $RNiO_3$ is also consistent with previous observations in $LaNiO_3/LaAlO_3$ SLs, where an emergent antiferromagnetic order was probed in the otherwise paramagnetic $LaNiO_3$ when the layer thickness was reduced to 2 uc.[13] Last but not least, we would like to point out that the thickness-independent T_N in $RNiO_3$ is in sharp contrast with the finite size effects observed in most antiferromagnetic materials and deserves further investigation.[51]

MITs in NNO/STO SLs with varied tetragonal distortions. To further address the effects of varied tetragonal distortions on the MITs, NNO/STO SLs with n = 5 were fabricated on $(001)_{pc}$-NGO (a_{pc} = 3.858 Å), (001)-$(LaAlO_3)_{0.3}(Sr_2AlTaO_6)_{0.7}$ (LSAT, a = 3.868 Å) and (001)-STO (a = 3.905 Å) substrates. RSM measurements confirm the fully strained state and same tetragonal symmetry for the three SLs (Supplementary Fig. 6). Their ρ-T curves are shown in Fig. 5a and the derived T_{MIT} and T_N are plotted as a function of the in-plane lattice parameter, a in Fig. 5d. The SLs grown on NGO and LSAT show very similar behavior, although the one on LSAT shows slightly higher T_{MIT} and T_N. By contrast, the greater tetragonal distortion imposed by STO substrate gives rise

to substantially increased T_{MIT}, T_N, as well as an enhanced resistivity jump across the MIT.

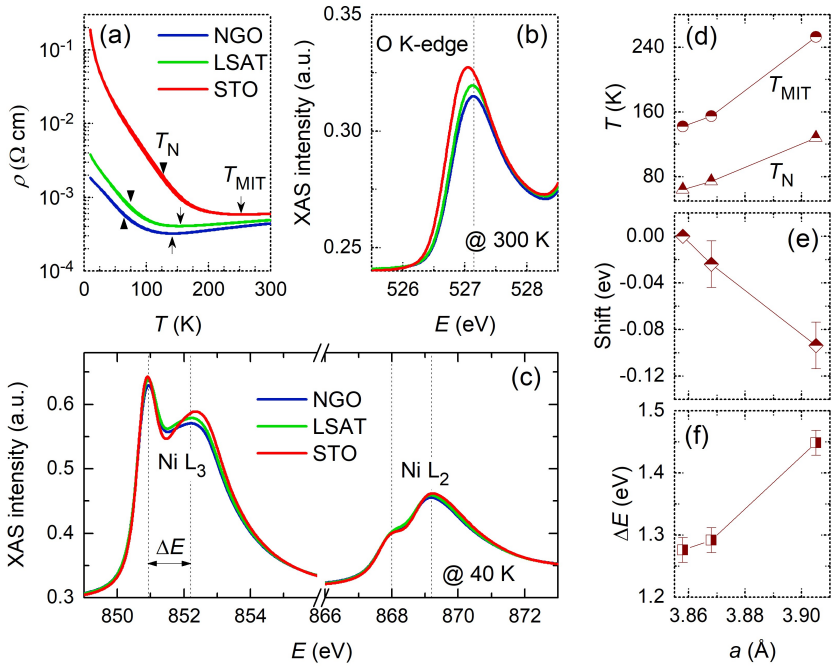

Fig. 5 MITs in NNO/STO SLs with varied tetragonal distortions. (a) ρ-T curves of the n = 5 SLs grown on various substrates. T_{MIT} and T_N are marked by arrows and triangles, respectively. (b) XAS spectra of the pre-peak of O K-edge at 300 K. (c) XAS spectra of Ni L-edge at 40 K. ΔE is the splitting energy of the double peaks of Ni L_3 edge. (d-f) summarizes T_{MIT} and T_N, energy shift of the O K-edge pre-peak relative to the SL grown on NGO(110), as well as ΔE as a function of the in-plane lattice constant, a.

To understand the varied MIT behaviors, the electronic structure was studied using x-ray absorption spectroscopy (XAS) performed at O K- and Ni L-edges. Fig. 5b shows the O K-edge pre-peak which arises from the strong covalency between Ni 3d and O 2p states. The peak position is determined by the charge transfer energy.[23,49,52] By taking the SL grown on NGO as a reference, the pre-peak shifts ~25 meV and ~95 meV to lower energy for the SLs grown on LSAT and STO, respectively (Fig. 5e). Such red shift of O K-edge pre-peak can be assigned to an increasing charge transfer energy when the SL is subjected to a larger in-plane tensile strain.[2,53] Fig. 5c shows XAS at Ni L-edge taken at 40 K, well below T_{MIT}. As can be seen, both Ni L_2 and L_3 edges split into two peaks,

resembling bulk RNiO$_3$.[52,54] We define ΔE as the energy separation of the two Ni L_3 peaks given the well-defined double-peak feature. ΔE increases from 1.27 eV on NGO to 1.29 eV on LSAT, and then to 1.45 eV on STO. The trend is in line with that of bulk RNiO$_3$ upon reducing the ion radius of R, indicating that the charge transfer energy and breathing distortions of NiO$_6$ octahedra increase with a.[52,54] Therefore, our results suggest that robust MITs can be triggered by imposing a large tetragonal distortion to NNO/STO SLs, albeit with strongly suppressed OOR.

Discussion

To summarize, we have demonstrated that the OOR of the NNO/STO SLs evolves from a modulated to uniform pattern as we gradually reduce the layer thickness of NNO. The altered OOR is found to profoundly influence the MIT and the antiferromagnetic transition temperatures. We observe a reduced T_{MIT} and T_N, together with a weakened insulating ground state as the OOR is suppressed. The dimensionality effects also play a role in the MIT which raises T_{MIT} by reducing the effective bandwidth. However, T_N is closely linked to the modifications of crystal structure, and insusceptible to the dimensional crossover. Our results illustrate that the delicate interplay between the spatial confinement and the interfacial OOR coupling can be utilized to engineer novel electronic phases at the atomic level.

Methods

Sample growth and characterization. The PLD depositions were conducted using a relatively high laser fluence of 2 J/cm^2 to insure the right stoichiometry of NNO.[46] The oxygen pressure and repetition rate were fixed at 0.2 mbar and 2 Hz, respectively. The substrate temperature was kept at 700 ºC. After the deposition, the samples were in-situ annealed for 15 min to improve the crystallinity before cooling down to room temperature. The single terminated NGO substrates were obtained by chemical etching with buffered HF, followed by annealing at 1050 ºC for 2 hours in oxygen flow.[55] The X-ray diffractions were performed on PANalytical-X'Pert materials research diffractometer

at the high-resolution mode. The surface morphology was characterized by atomic force microscopy. Transport properties were measured using a van der Pauw geometry on the Quantum Design physical property measurement system.

Scanning transmission electron microscopy. The characterization of the atomic structure was conducted using Cs-corrected scanning transmission electron microscopy high angle dark field imaging (STEM-HAADF) on the X-Ant-Em instrument at the University of Antwerp operated at 300kV, a convergence angle of 20 mrad and a collection angle of 44-190 mrad. The samples were cut along the orthorhombic [001] direction of NGO substrates using a FEI Helios 650 dual-beam Focused Ion Beam device. Chemical mapping was performed using electron energy loss spectroscopy (EELS) on a Gatan Quantum ERS spectrometer with a collection angle of 85 mrad, an exposure time of 80 ms/pixel and a 0.5 eV/pixel dispersion in dual EELS mode. Raw data is presented after power-law background subtraction.

Resonant magnetic diffraction. The RMD experiments were performed using an in-vacuum 4-circle diffractometer with chamber pressure below 10^{-9} Torr at the resonant elastic and inelastic X-ray scattering beamline at Canadian light source in Saskatoon, Canada. The beamline has a flux of 5×10^{12} photon s^{-1} and energy resolution of 10^{-4} eV.

X-ray absorption spectroscopy. The XAS experiments were performed at the X-Treme beamline of the Swiss Light Source.[56] The data were collected using the total electron yield mode, with incoming X-ray at an angle of 30° from the sample surface. The spectra shown in Fig.5 were obtained by averaging four successive spectra measured with π and σ linear polarizations.

References

(1) Schlom, D. G.; Chen, L.-Q.; Fennie, C. J.; Gopalan, V.; Muller, D. A.; Pan, X.; Ramesh, R.; Uecker, R. Elastic strain engineering of ferroic oxides. *MRS Bull.*, **39**, 118-130 (2014).

(2) Liu, J.; Kargarian, M.; Kareev, M.; Gray, B.; Ryan, P. J.; Cruz, A.; Tahir, N.; Chuang, Y.-D.; Guo, J.; Rondinelli, J. M.; Freeland, J. W.; Fiete, G. A.; Chakhalian, J. Heterointerface engineered electronic and magnetic phases of $NdNiO_3$ thin films. *Nat. Commun.* **4**, 2714 (2013).

(3) Rondinelli, J. M.; May, S. J.; Freeland, J. W. Control of octahedral connectivity in perovskite oxide heterostructures: An emerging route to multifunctional materials discovery. *MRS Bull.* **37**, 261-270 (2012).

(4) Rondinelli, J. M.; Spaldin, N. A. Structure and properties of functional oxide thin films:

Insights from electronic-structure calculations. *Adv. Mater.* **23**, 3363-3381 (2011).
(5) Liao, Z.; Huijben, M.; Zhong, Z.; Gauquelin, N.; Macke, S.; Green, R. J.; Van Aert, S.; Verbeeck, J.; Van Tendeloo, G.; Held, K.; Sawatzky, G. A.; Koster, G.; Rijnders, G. Controlled lateral anisotropy in correlated manganite heterostructures by interface-engineered oxygen octahedral coupling. *Nat. Mater.* **15**, 425-431 (2016).
(6) Kan, D.; Aso, R.; Sato, R.; Haruta, M.; Kurata, H.; Shimakawa, Y. Tuning magnetic anisotropy by interfacially engineering the oxygen coordination environment in a transition metal oxide. *Nat. Mater.* **15**, 432-437 (2016).
(7) Moon, E. J.; Colby, R.; Wang, Q.; Karapetrova, E.; Schlepütz, C. M.; Fitzsimmons, M. R.; May, S. J. Spatial control of functional properties via octahedral modulations in complex oxide superlattices. *Nat. Commun.* **5**, 5710 (2014).
(8) Moon, E. J.; Balachandran, P. V.; Kirby, B. J.; Keavney, D. J.; Sichel-Tissot, R. J.; Schlepütz, C. M.; Karapetrova, E.; Cheng, X. M.; Rondinelli, J. M.; May, S. J. Effect of interfacial octahedral behavior in ultrathin manganite films. *Nano Lett.* **14**, 2509-2514 (2014).
(9) Liao, Z.; Gauquelin, N.; Green, R. J.; Müller-Caspary, K.; Lobato, I.; Lin, L.; Van Aert, S.; Verbeeck, J.; Huijben, M.; Grisolia, M. N.; Rouco, V.; El Hage, R.; Villegas, J. E.; Mercy, A.; Bibes, M.; Ghosez, P.; Sawatzky, G. A.; Rijnders, G.; Koster, G. Metal-insulator-Transition engineering by modulation tilt-control in perovskite nickelates for room temperature optical switching. *Proc. Natl. Acad. Sci.* **115**, 9515-9520 (2018).
(10) Liao, Z.; Green, R. J.; Gauquelin, N.; Macke, S.; Li, L.; Gonnissen, J.; Sutarto, R.; Houwman, E. P.; Zhong, Z.; Van Aert, S.; Verbeeck, J.; Sawatzky, G. A.; Huijben, M.; Koster, G.; Rijnders, G. Long-range domain structure and symmetry engineering by interfacial oxygen octahedral coupling at heterostructure interface. *Adv. Funct. Mater.* **26**, 6627-6634 (2016).
(11) Bousquet, E.; Dawber, M.; Stucki, N.; Lichtensteiger, C.; Hermet, P.; Gariglio, S.; Triscone, J.-M.; Ghosez, P. Improper ferroelectricity in perovskite oxide artificial superlattices. *Nature* **452**, 732-736 (2008).
(12) May, S. J.; Smith, C. R.; Kim, J. W.; Karapetrova, E.; Bhattacharya, A.; Ryan, P. J. Control of octahedral rotations in $(LaNiO_3)_n/(SrMnO_3)_m$ superlattices. *Phys. Rev. B* **83**, 153411 (2011).
(13) Boris, A. V.; Matiks, Y.; Benckiser, E.; Frano, A.; Hinkov, V.; Wochner, P.; Castro-Colin, M.; Detemple, E.; Malik, V. K.; Bernhard, C.; Prokscha, T.; Suter, A.; Salman, Z.; Morenzoni, E.; Cristiani, G.; Habermeier, H.-U.; Keimer, B. Dimensionality control of electronic phase transitions in nickel-oxide superlattices. *Science* **332**, 937-940 (2011).
(14) Sakai, E.; Tamamitsu, M.; Yoshimatsu, K.; Okamoto, S.; Horiba, K.; Oshima, M.; Kumigashira, H. Gradual localization of Ni 3*d* states in $LaNiO_3$ ultrathin films induced by dimensional crossover. *Phys. Rev. B* **87**, 075132 (2013).
(15) King, P. D. C.; Wei, H. I.; Nie, Y. F.; Uchida, M.; Adamo, C.; Zhu, S.; He, X.; Božović, I.; Schlom, D. G.; Shen, K. M. Atomic-scale control of competing electronic phases in ultrathin $LaNiO_3$. *Nat. Nanotechnol.* **9**, 443-447 (2014).
(16) Sakai, E.; Yoshimatsu, K.; Tamamitsu, M.; Horiba, K.; Fujimori, A.; Oshima, M.; Kumigashira, H. Bandwidth-controlled metal-insulator transition in epitaxial $PrNiO_3$ ultrathin films induced by dimensional crossover. *Appl. Phys. Lett.* **104**, 171609 (2014).
(17) Wang, L.; Ju, S.; You, L.; Qi, Y.; Guo, Y. W.; Ren, P.; Zhou, Y.; Wang, J. Competition between strain and dimensionality effects on the electronic phase transitions in $NdNiO_3$ films. *Sci. Rep.* **5**, 18707 (2015).
(18) Chen, P. F.; Chen, B. B.; Tan, X. L.; Xu, H. R.; Xuan, X. F.; Guo, Z.; Jin, F.; Wu, W. B. High- T_C ferromagnetic order in $CaRuO_3/La_{2/3}Ca_{1/3}MnO_3$ superlattices. *Appl. Phys. Lett.* **103**, 262402 (2013).
(19) Chen, B.; Chen, P.; Xu, H.; Jin, F.; Guo, Z.; Lan, D.; Wan, S.; Gao, G.; Chen, F.; Wu, W.

Interfacial control of ferromagnetism in ultrathin $La_{0.67}Ca_{0.33}MnO_3$ sandwiched between $CaRu_{1-x}Ti_xO_3$ (x = 0-0.8) epilayers. *ACS Appl. Mater. Interfaces* **8**, 34924-34932 (2016).
(20) Qiao, L.; Jang, J. H.; Singh, D. J.; Gai, Z.; Xiao, H.; Mehta, A.; Vasudevan, R. K.; Tselev, A.; Feng, Z.; Zhou, H.; Li, S.; Prellier, W.; Zu, X.; Liu, Z.; Borisevich, A.; Baddorf, A. P.; Biegalski, M. D. Dimensionality controlled octahedral symmetry-mismatch and functionalities in epitaxial $LaCoO_3/SrTiO_3$ heterostructures. *Nano Lett.* **15**, 4677-4684 (2015).
(21) Schütz, P.; Di Sante, D.; Dudy, L.; Gabel, J.; Stübinger, M.; Kamp, M.; Huang, Y.; Capone, M.; Husanu, M.-A.; Strocov, V. N.; Sangiovanni, G.; Sing, M.; Classen, R. Dimensionality-driven metal-insulator transition in spin-orbit-coupled $SrIrO_3$. *Phys. Rev. Lett.* **119**, 256404 (2017).
(22) Catalan, G. Progress in perovskite nickelate research. *Phase Transitions* **81**, 729-749 (2008).
(23) Middey, S.; Chakhalian, J.; Mahadevan, P.; Freeland, J. W.; Millis, A. J.; Sarma, D. D. Physics of ultrathin films and heterostructures of rare earth nickelates. Annu. Rev. Mater. Res. **46**, 305-334 (2016).
(24) Alonso, J. A.; García-Muñoz, J. L.; Fernández-Díaz, M. T.; Aranda, M. A. G.; Martínez-Lope, M. J.; Casais, M. T. Charge disproportionation in $R$$NiO_3$ perovskites: simultaneous metal-insulator and structural transition in $YNiO_3$. *Phys. Rev. Lett.* **82**, 3871-3874 (1999).
(25) Mizokawa, T.; Khomskii, D. I.; Sawatzky, G. A. Spin and charge ordering in self-doped Mott insulators. *Phys. Rev. B* **61**, 11263 (2000).
(26) Stewart, M. K.; Liu, J.; Kareev, M.; Chakhalian, J.; Basov, D. N. Mott physics near the insulator-to-metal transition in $NdNiO_3$. *Phys. Rev. Lett.* **107**, 176401 (2011).
(27) Johnston, S.; Mukherjee, A.; Elfimov, I.; Berciu, M.; Sawatzky, G. A. Charge disproportionation without charge transfer in the rare-earth-element nickelates as a possible mechanism for the metal-insulator transition. *Phys. Rev. Lett.* **112**, 106404 (2014).
(28) Upton, M. H.; Choi, Y.; Park, H.; Liu, J.; Meyers, D.; Chakhalian, J.; Middey, S.; Kim, J.-W.; Ryan, P. J. Novel electronic behavior driving $NdNiO_3$ metal-insulator transition. *Phys. Rev. Lett.* **115**, 036401 (2015).
(29) Mercy, A.; Bieder, J.; Íñiguez, J.; Ghosez, P. Structurally triggered metal-insulator transition in rare-earth nickelates. *Nat. Commun.* **8**, 1677 (2017).
(30) Varignon, J.; Grisolia, M. N.; Íñiguez, J.; Barthélémy, A.; Bibes, M. Complete phase diagram of rare-earth nickelates from first-principles. *npj Quantum Mater.***2**, 21 (2017).
(31) Bisogni, V.; Catalano, S.; Green, R. J.; Gibert, M.; Scherwitzl, R.; Huang, Y.; Strocov, V. N.; Zubko, P.; Balandeh, S.; Triscone, J.-M.; Sawatzky, G.; Schmitt, T. Ground-state oxygen holes and the metal-insulator transition in the negative charge-transfer rare-earth nickelates. *Nat. Commun.* **7**, 13017 (2016).
(32) Chaloupka, J.; Khaliullin, G. Orbital order and possible superconductivity in $LaNiO_3/LaMO_3$ superlattices. *Phys. Rev. Lett.* **100**, 016404 (2008).
(33) Hansmann, P.; Yang, X.; Toschi, A.; Khaliullin, G.; Andersen, O. K.; Held, K. Turning a nickelate Fermi surface into a cupratelike one through heterostructuring. *Phys. Rev. Lett.* **103**, 016401 (2009).
(34) Liu, J.; Kareev, M.; Meyers, D.; Gray, B.; Ryan, P.; Freeland, J. W.; Chakhalian, J. Metal-insulator transition and orbital reconstruction in Mott-type quantum wells made of $NdNiO_3$. *Phys. Rev. Lett.* **109**, 107402 (2012).
(35) Scherwitzl, R.; Gariglio, S.; Gabay, M.; Zubko, P.; Gibert, M.; Triscone, J.-M. Metal-insulator transition in ultrathin $LaNiO_3$ films. *Phys. Rev. Lett.* **106**, 246403 (2011).
(36) Miao, N.; Bristowe, N. C.; Xu, B.; Verstraete, M. J.; Ghosez, P. First-principles study of the lattice dynamical properties of strontium ruthenate. *J. Phys. Condens. Matter*. **26** 035401 (2014).
(37) Zhang, J. Y.; Hwang, J.; Raghavan, S.; Stemmer, S. Symmetry lowering in extreme-

electron-density perovskite quantum wells. *Phys. Rev. Lett.* **110**, 256401 (2013).
(38) Zhang, J. Y.; Kim, H.; Mikheev, E.; Hauser, A. J.; Stemmer, S. Key role of lattice symmetry in the metal-insulator transition of $NdNiO_3$ films. *Sci. Rep.* **6**, 23652 (2016).
(39) Vailionis, A.; Boschker, H.; Siemons, W.; Houwman, E. P.; Blank, D. H. A.; Rijnders, G.; Koster, G. Misfit strain accommodation in epitaxial ABO_3 perovskites: lattice rotations and lattice modulations. *Phys. Rev. B* **83**, 064101 (2011).
(40) Chang, S. H.; Chang, Y. J.; Jang, S. Y.; Jeong, D. W.; Jung, C. U.; Kim, Y. J.; Chung, J. S.; Noh, T. W. Thickness-dependent structural phase transition of strained $SrRuO_3$ ultrathin films: The role of octahedral tilt. *Phys. Rev. B* **84**, 104101 (2011).
(41) Kan, D.; Wakabayashi, Y.; Tajiri, H.; Shimakawa, Y. Interfacially engineered oxygen octahedral rotations and their impact on strain relief in coherently grown $SrRuO_3$ films. *Phys. Rev. B* **94**, 024112 (2016).
(42) Vailionis, A.; Boschker, H.; Liao, Z.; Smit, J. R. A.; Rijnders, G.; Huijben, M.; Koster, G. Symmetry and lattice mismatch induced strain accommodation near and away from correlated perovskite interfaces. *Appl. Phys. Lett.* **105**, 131906 (2014).
(43) Hwang, J.; Son, J.; Zhang, J. Y.; Janotti, A.; Van De Walle, C. G.; Stemmer, S. Structural origins of the properties of rare earth nickelate superlattices. *Phys. Rev. B* **87**, 060101 (2013).
(44) Son, J.; Lebeau, J. M.; Allen, S. J.; Stemmer, S. Conductivity enhancement of ultrathin $LaNiO_3$ films in superlattices. *Appl. Phys. Lett.* **97**, 202109 (2010).
(45) Xiang, P.-H.; Zhong, N.; Duan, C.-G.; Tang, X. D.; Hu, Z. G.; Yang, P. X.; Zhu, Z. Q.; Chu, J. H. Strain controlled metal-insulator transition in epitaxial $NdNiO_3$ thin films. *J. Appl. Phys.* **114**, 243713 (2013).
(46) Breckenfeld, E.; Chen, Z.; Damodaran, A. R.; Martin, L. W. Effects of nonequilibrium growth, nonstoichiometry, and film orientation on the metal-to-insulator transition in $NdNiO_3$ thin films. *ACS Appl. Mater. Interfaces* **6**, 22436-22444 (2014).
(47) Zhou, J. S.; Goodenough, J. B.; Dabrowski, B. Exchange interaction in the insulating phase of $RNiO_3$. *Phys. Rev. Lett.* **95**, 127204 (2005).
(48) Middey, S.; Meyers, D.; Kareev, M.; Cao, Y.; Liu, X.; Shafer, P.; Freeland, J. W.; Kim, J.-W.; Ryan, P. J.; Chakhalian, J. Disentangled cooperative orderings in artificial rare-earth nickelates. *Phys. Rev. Lett.* **120**, 156801 (2018).
(49) Disa, A. S.; Georgescu, A. B.; Hart, J. L.; Kumah, D. P.; Shafer, P.; Arenholz, E.; Arena, D. A.; Ismail-Beigi, S.; Taheri, M. L.; Walker, F. J.; Ahn, C. H. Control of hidden ground-state order in $NdNiO_3$ superlattices. Phys. Rev. Mater. **1**, 024410 (2017).
(50) Catalan, G.; Bowman, R. M.; Gregg, J. M. Metal-insulator transitions in $NdNiO_3$ thin films. Phys. Rev. B **62**, 7892 (2000).
(51) Ambrose, T.; Chien, C. L. Finite-size effects and uncompensated magnetization in thin antiferromagnetic CoO layers. *Phys. Rev. Lett.* **76**, 1743 (1996).
(52) Freeland, J. W.; Van Veenendaal, M.; Chakhalian, J. Evolution of electronic structure across the rare-earth $RNiO_3$ series. *J. Electron Spectros. Relat. Phenomena* **208**, 56-62 (2016).
(53) Chakhalian, J.; Rondinelli, J. M.; Liu, J.; Gray, B. A.; Kareev, M.; Moon, E. J.; Prasai, N.; Cohn, J. L.; Varela, M.; Tung, I. C.; Bedzyk, M. J.; Altendorf, S. G.; Strigari, F.; Dabrowski, B.; Tjeng, L. H.; Ryan, P. J.; Freeland, J. W. Asymmetric orbital-lattice interactions in ultrathin correlated oxide films. *Phys. Rev. Lett.* **107**, 116805 (2011).
(54) Piamonteze, C.; de Groot, F. M. F.; Tolentino, H. C. N.; Ramos, A. Y.; Massa, N. E.; Alonso, J. A.; Martínez-Lope, M. J. Spin-orbit-induced mixed-spin ground state in $R NiO_3$ perovskites probed by x-ray absorption spectroscopy: Insight into the metal-to-insulator transition *Phys. Rev. B* **71**, 020406(R) (2005).
(55) Leca, V.; Blank, D. H. A.; Rijnders, G. Termination control of $NdGaO_3$ crystal surfaces by selective chemical etching. arXiv:1202.2256v2 (2012).

(56) Piamonteze, C.; Flechsig, U.; Rusponi, S.; Dreiser, J.; Heidler, J.; Schmidt, M.; Wetter, R.; Calvi, M.; Schmidt, T.; Pruchova, H.; Krempasky, J.; Quitmann, C.; Brune, H.; Nolting, F. X-Treme beamline at SLS: X-ray magnetic circular and linear dichroism at high field and low temperature. *J. Synchrotron Radiat.* **19**, 661–674 (2012).

Acknowledgements

This work is supported by the international M-ERA.NET project SIOX (project 4288). J.V. and N.G. acknowledge funding through the GOA project "Solarpaint" of the University of Antwerp. The microscope used in this work was partly funded by the Hercules Fund from the Flemish Government. D.J. acknowledges funding from FWO project G093417N from the Flemish fund for scientific research. M. S. acknowledges funding from Slovenian Research Agency (grants J2-9237 and P2-0091). R.J.G. acknowledges funding from the Natural Sciences and Engineering Research Council of Canada (NSERC). Part of the research described in this paper was performed at the Canadian Light Source, a national research facility of the University of Saskatchewan, which is supported by the Canada Foundation for Innovation (CFI), NSERC, the National Research Council (NRC), the Canadian Institutes of Health Research (CIHR), the Government of Saskatchewan, and the University of Saskatchewan.

Author contributions

B.C. synthesized the samples and conducted the basic structural characterizations and transport measurements. N.G. and D.J. performed STEM measurements and analyses under the supervision of J.V. R.G. performed RMD measurements. B.C. performed XAS measurements assisted by C.P. B.C., N.G., M.S., M.H., G.R. and G.K. discussed the results. B.C. and G.K. conceived the project and wrote the manuscript with inputs from all authors.

Additional information

Supplementary Information accompanying this paper can be found online.